


ARTICLE

<https://doi.org/10.1038/s41467-019-09384-7>

OPEN

A polymer-direct-intercalation strategy for MoS₂/carbon-derived heteroerogels with ultrahigh pseudocapacitance

Nan Feng^{1,2}, Ruijin Meng^{1,2}, Lianhai Zu¹, Yutong Feng¹, Chengxin Peng³, Jimei Huang¹, Guanglei Liu¹, Bingjie Chen¹ & Jinhu Yang ^{1,2}

The intercalation strategy has become crucial for 2D layered materials to achieve desirable properties, however, the intercalated guests are often limited to metal ions or small molecules. Here, we develop a simple, mild and efficient polymer-direct-intercalation strategy that different polymers (polyethyleneimine and polyethylene glycol) can directly intercalate into the MoS₂ interlayers, forming MoS₂-polymer composites and interlayer-expanded MoS₂/carbon heteroerogels after carbonization. The polymer-direct-intercalation behavior has been investigated by substantial characterizations and molecular dynamic calculations. The resulting composite heteroerogels possess 3D conductive MoS₂/C frameworks, expanded MoS₂ interlayers (0.98 nm), high MoS₂ contents (up to 74%) and high Mo valence (+6), beneficial to fast and stable charge transport and enhanced pseudocapacitive energy storage. Consequently, the typical MoS₂/N-doped carbon heteroerogels exhibit outstanding supercapacitor performance, such as ultrahigh capacitance, remarkable rate capability and excellent cycling stability. This study offers a new intercalation strategy which may be generally applicable to 2D materials for promising energy applications.

¹School of Chemical Science and Engineering, Tongji University, Shanghai 200092, China. ²Research Center for Translational Medicine and Key Laboratory of Arrhythmias of the Ministry of Education of China, East Hospital Tongji University School of Medicine, No. 150 Jimo Road, Shanghai 200120, China.

³School of Materials Science and Engineering, University of Shanghai for Science and Technology, Shanghai 200093, China. These authors contributed equally: Nan Feng, Ruijin Meng. Correspondence and requests for materials should be addressed to J.Y. (email: yangjinhu@tongji.edu.cn)

To meet ever-increasing energy demands, the exploration of advanced electrode materials has been triggered for developing state-of-the-art energy storage devices. Among various energy storage devices, supercapacitors are promising due to ultrahigh power output and ultralong operating lifetime¹. There are two different working mechanisms in supercapacitors, including electrochemical double layer capacitive (EDLC) energy storage^{2,3} and pseudocapacitive (PC) energy storage⁴. The first mechanism is realized through physically adsorbing opposing electrolyte charges in two electrodes, featuring high power and long cycling life, while the latter relates to fast and reversible redox reactions occurring over electrodes, significantly elevating the capacitance and meanwhile maintaining high rate capability. The mechanisms are largely determined by the electrode materials employed and play a decisive role in the performance of supercapacitors. When the two mechanisms work together in a supercapacitor, a high comprehensive performance is expected due to their synergistic effect. However, supercapacitors are still suffering from low energy densities, which is an obstacle for their practical applications. Current efforts mainly focus on the development of high-capacitance supercapacitors with simultaneous high power. To achieve high specific capacitance, electrode materials should be designed with high porosity, good electrical conductivity, and especially, feasible redox reactions for efficient PC energy storage.

Recently, MoS₂ nanosheets, an analogue of graphene with a two-dimensional layered nanostructure, have attracted tremendous attention for supercapacitors due to their unique structural and electronic properties^{5–7}. Specifically, MoS₂ nanosheets are stacked by S–Mo–S monolayers via weak van der Waals forces along the *c* axis, which allows easy intercalation of foreign ions (H⁺, K⁺, NH₄⁺) for interlayer charge storage⁸. In addition, the central Mo ions hold a range of oxidation states from +2 to +6, exhibiting great potential in high-capacitance PC storage⁹. However, the performance of MoS₂-based supercapacitors is still limited by the poor electrical conductivity and few accessible active sites of MoS₂. Considerable efforts have been made to either improve the conductivity of MoS₂ by integrating conductive carbon materials (graphene^{10–13}, carbon nanotubes^{14–17}, and conducting polymers^{18–20}), or expose more active sites of MoS₂ nanosheets through intercalation using small molecules or ions. In particular, further strategies combining the above mentioned two solutions to simultaneously increase conductivity and extended interlayer of MoS₂ have also been developed for the preparation of MoS₂/carbon composites^{21,22}. Conventionally, the synthesis strategies can be categorized as “top-down” and “bottom-up” by employing polymers as both carbon sources and intercalation agents, as depicted in Fig. 1a, b. The “top-down” strategy involves the first exfoliation of existing MoS₂ by intercalation of small molecules or ions, followed by the mixing and restacking of MoS₂ monolayers and polymers, which often accompanies with the formation of highly unstable and flammable intermediates^{15,23–27}. The “bottom-up” strategy was realized through the in situ nucleation and growth of MoS₂ monolayers on polymer molecules (polyaniline, polyvinyl pyrrolidone, polyethylene oxide, etc.), which requires precise control of polymer-mediated crystal growth in thermodynamics and dynamics to avoid the formation of bulk MoS₂ and phase separation between MoS₂ and polymers^{28–35}. Despite great progress, it is noted that the conventional strategies are often associated with complicated approaches such as extra intercalation manipulation or harsh growth conditions. In addition, the resulting MoS₂/carbon composites are usually in the form of powders, especially when the MoS₂ active material is in high content (over 50%) in the composites, which may lead to a high contacting resistance as well as an unstable and ineffective ion

diffusion pathway caused by the aggregation of MoS₂. Therefore, it is highly desirable to develop a new, simple, and efficient strategy for constructing MoS₂/carbon composites with architectures/nanostructures that are favorable for high-performance supercapacitors.

In this work, we propose a novel polymer-direct-intercalation (PDI) strategy to construct three-dimensional (3D) MoS₂/N-doped carbon (MoS₂/NC) composite hetero-aerogels assembled by layered MoS₂/carbon heteronanosheets for ultrahigh-capacitance supercapacitors. The strategy, which is simple, mild, and efficient, is realized at room temperature by direct intercalation of polymer molecules into the interlayers of prepared MoS₂ nanosheets (Fig. 1c), followed by carbonization treatment. The resulting MoS₂/NC hetero-aerogels possess a 3D conductive N-doped MoS₂/C framework, an overlapped MoS₂/C-layered hetero-interface and expanded interlayers of MoS₂ nanosheets, conducive not only to fast and stable charge transfer/diffusion, but also enhanced ion intercalation pseudocapacitance. Moreover, when employed as electrodes for supercapacitors, the MoS₂/NC hetero-aerogel with a high content of MoS₂ (up to 74%) and a high valence (+6) of central Mo ions can deliver an ultrahigh specific capacitance of 4144 F g⁻¹ at 1 A g⁻¹, remarkable rate capability (2483 F g⁻¹ at a drastically increased current density of 10 A g⁻¹), and excellent cycling stability with a capacitance loss of ~8% after 8000 cycles at 10 A g⁻¹.

Results

Synthesis of the MoS₂/N-doped carbon hetero-aerogel. Figure 1d shows the typical preparation procedure of the MoS₂/NC composite aerogel by polymer (polyethyleneimine, PEI, Mw = 600, 1800, 10,000, 70,000) direct intercalation. First, pre-intercalated MoS₂ nanosheets with interlayer distance of ~10.0 Å were synthesized hydrothermally with the assistance of ammonium and then were mixed with PEI at room temperature for intercalation. It is noted that the pre-intercalated MoS₂ nanosheets are in the form of powder and can be produced in a large amount. The pre-intercalated MoS₂ nanosheets are intertwined and stacked into a 3D network (scanning electron microscope (SEM) image, inset in Fig. 1e) with a relatively high specific surface area of ~99.99 m² g⁻¹ (Supplementary Fig. 1a). The pre-intercalated MoS₂ nanosheets were detected to possess a negative charge surface (zeta potential -30.4 mV, Supplementary Fig. 2) in neutral aqueous solution. Therefore, PEI was preferentially selected as the intercalator owing to the strong electrostatic interaction between its positively charged NH₂⁺ groups and negatively charged MoS₂ nanosheets. As a result, PEI molecules readily adsorbed on the surface of MoS₂ nanosheets and inserted into the interlayers of MoS₂ nanosheets assisted with the ultrasonic treatment. With intercalation, an aerogel-like 3D MoS₂-PEI (PEI, Mw = 600) composite instead of powder was formed after freeze-drying due to the linkage of PEI molecules between MoS₂ nanosheets, showing a cylinder-like shape with a diameter of ~2.5 cm and a height of ~3 cm (Fig. 1f). The coating of PEI on MoS₂ nanosheets was clearly visible (inset of Fig. 1f). Finally, the MoS₂/NC hetero-aerogel with the expanded MoS₂ interlayers was obtained through in situ transformation of the MoS₂-PEI composite at 800 °C. The shape of the MoS₂/NC hetero-aerogel was well preserved compared with its MoS₂-PEI precursor, despite slight volume shrinkage (Fig. 1g). The tap density of the MoS₂/NC hetero-aerogel was calculated to be approximately 0.1263 g cm⁻³, which makes the aerogel stand freely on a *Fatsia japonica* flower³⁶. Furthermore, thanks to a variety of stacked pores, the MoS₂/NC hetero-aerogel exhibits a 3D porous architecture (inset of Fig. 1g) and possesses a specific surface area of ~120.4 m² g⁻¹ (Supplementary Fig. 1b), slightly higher than that of the pure MoS₂ due possibly to more exposed interlayer surface

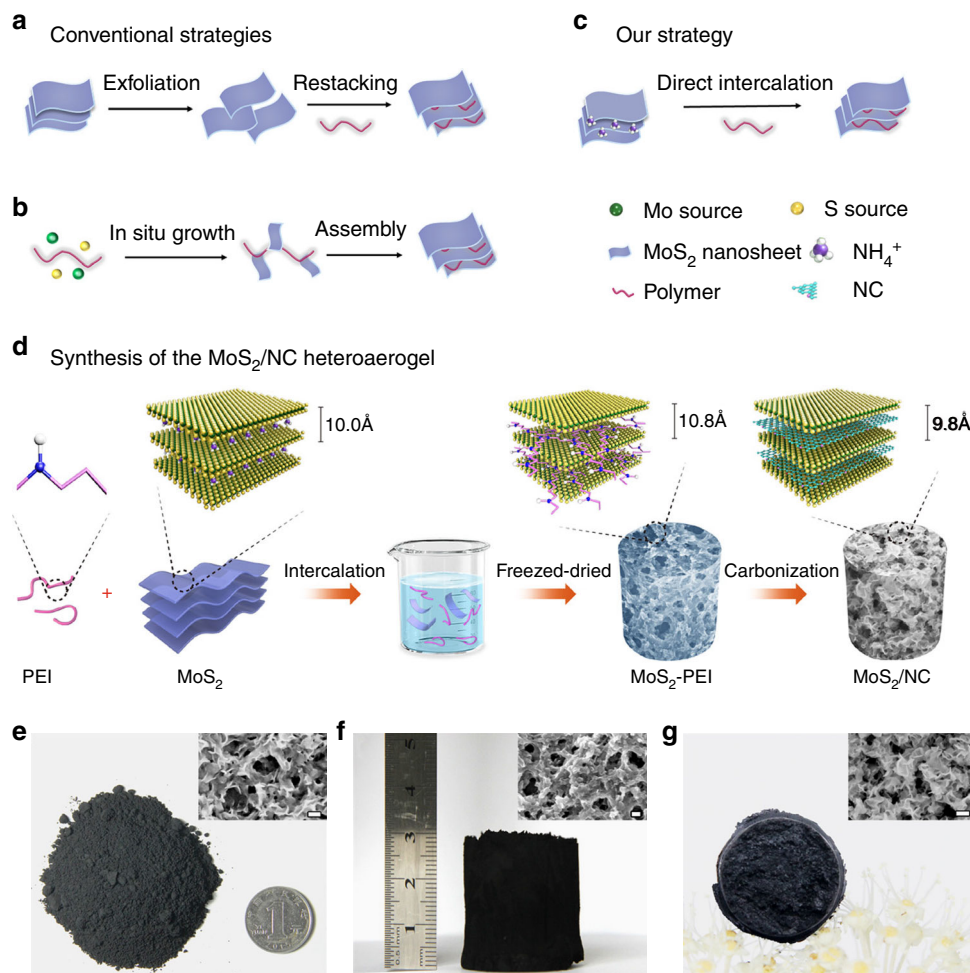


Fig. 1 Comparison of different strategies and the polymer direct intercalation. **a–c** The schematic illustrations show the conventional synthetic strategies to realize interlayer-expanded MoS₂ (**a**, **b**) and the polymer-direct-intercalation (PDI) strategy for the synthesis of a MoS₂/NC hetero-aerogel (**c**) to prepare interlayer-expanded MoS₂/carbon composites. **d** The schematic illustration for the synthetic procedure of the MoS₂/NC hetero-aerogel. **e–g** Optical photographs of the as-synthesized pre-intercalated MoS₂ nanosheets (**e**), the MoS₂-PEI (PEI, Mw = 600) composite after freeze-drying (**f**), and the MoS₂/NC hetero-aerogel after carbonization (**g**). Insets of (**e–g**) show the corresponding SEM images with scale bars of 100 nm

through the intercalation and the contribution of the carbon component.

Structure and composition of the MoS₂/N-doped carbon hetero-aerogel. A high-resolution transmission electron microscopy (HRTEM) image of the MoS₂/NC hetero-aerogel in Fig. 2a shows that MoS₂ nanosheets are in few layers, showing a tangled and distorted morphology with an expanded interlayer distance of ~0.98 nm, which confirms a graphene-like carbon monolayer inserting into MoS₂ interlayers³⁰. The possible mechanism forming graphene-like carbon monolayers in the MoS₂ interlayers after carbonization is discussed (Supplementary Note 1). In addition, a thin carbon layer is also observed on the surface of MoS₂ nanosheets induced by the adsorption and subsequent in situ carbonization of PEI on MoS₂ nanosheets, indicating the formation of an interconnected network of graphitized carbon throughout the hetero-aerogel. It is also found that the crystal lattices in (002) plane of MoS₂ nanosheets also are distorted to some extent, caused by the introducing foreign atoms (N, C) onto the surface or into interlayers of MoS₂ nanosheets, as shown in Fig. 2b. Figure 2c shows the TEM image of pristine MoS₂ nanosheets obtained after thermal treatment. Differently, the MoS₂ nanosheets show a clean surface, consisting of orderly arranged thin monolayers with a normal displacing of ~0.62 nm

for (002) plane^{10,37}. In addition, a regular atomic arrangement in (002) plane with the lattice distance of 0.25 nm, corresponding to the (101) plane of MoS₂³⁰ (Fig. 2d). The results above indicate that the graphitized carbon stably exists both in the interlayers and on the surface of MoS₂ nanosheets through the direct intercalation of PEI. We further employed energy dispersive X-ray spectrometry (EDS) to analyze the chemical composition of the MoS₂/NC hetero-aerogel. EDS data reveals that Mo, S, C, and N elements coexist and distribute uniformly throughout the whole hetero-aerogel (Supplementary Figs. 3, 2e), further verifying the successful formation of the MoS₂/NC hetero-aerogel. The above results demonstrate that the direct intercalation strategy is effective, which enables not only the adsorption of PEI molecules onto MoS₂ nanosheets, but also the intercalation into the interlayers of MoS₂ nanosheets. The PEI molecules on the surface of MoS₂ nanosheets in the MoS₂-polymer composites serve as an interconnected polymer chain network to stabilize the shape and structure of the aerogel-like MoS₂-polymer composites. After carbonization, these interconnected PEI molecules converted in situ to graphitized carbon layers on the surface of MoS₂ and interconnected carbon networks, accompanying with the formation of the MoS₂/NC hetero-aerogels.

To systematically investigate the PEI direct-intercalation behaviors, X-ray diffraction (XRD) characterization was applied

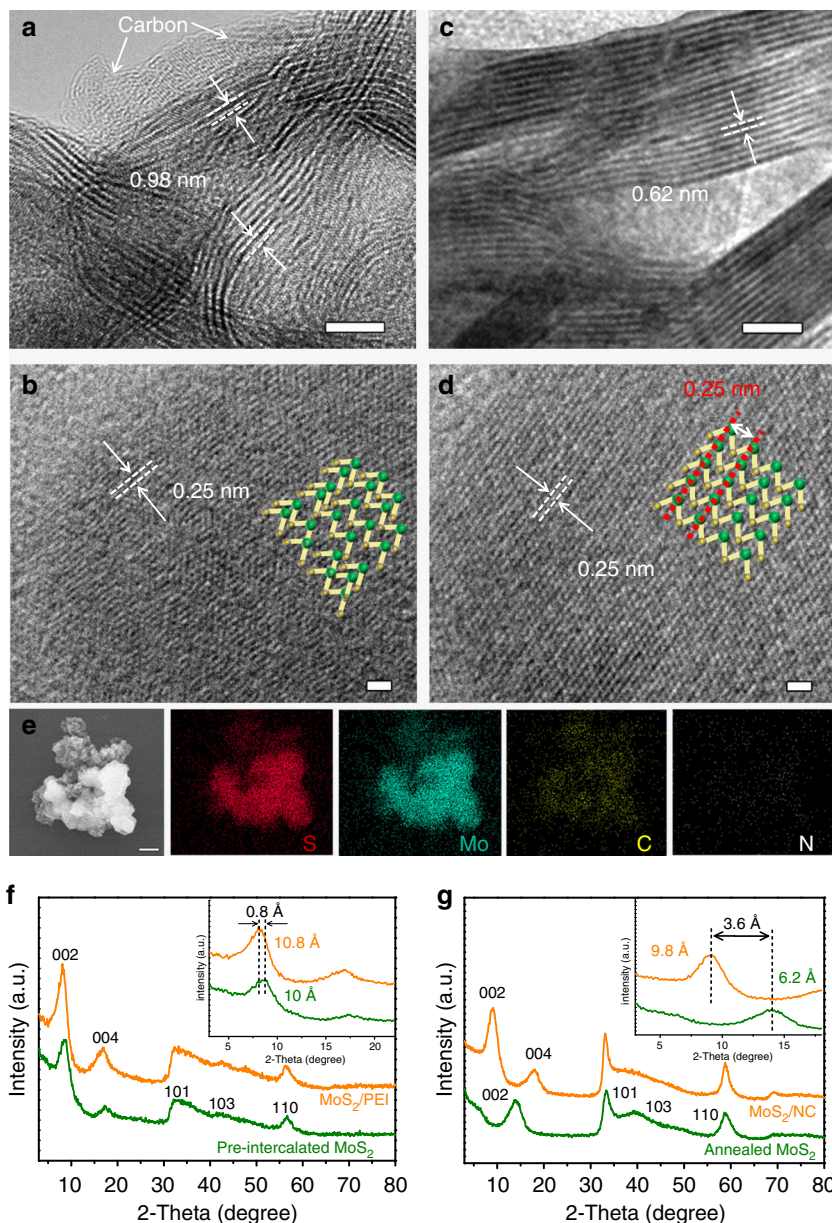


Fig. 2 Characterization of the MoS₂/NC hetero-aerogel and MoS₂ nanosheets. **a–d** TEM images of the MoS₂/NC hetero-aerogel derived from the intercalation of PEI (*M_w* = 600) (**a, b**) and the annealed MoS₂ nanosheets (**c, d**). Insets of (**b, d**) show the corresponding SAED patterns. **e** SEM-EDS mapping images of the MoS₂/NC hetero-aerogel. **f** XRD patterns of the MoS₂ nanosheets and MoS₂-PEI composite obtained after freeze-drying. **g** XRD patterns of MoS₂/NC hetero-aerogel obtained after thermal treatments. Scale bars: **a, c** 5 nm; **b, d** 1 nm; **e** 1 μm

to the pre-intercalated MoS₂ nanosheets and MoS₂-PEI composite, as well as their corresponding annealed MoS₂ nanosheets and carbonized products of the MoS₂/NC hetero-aerogel (Fig. 2f, g). The pre-intercalated MoS₂ and the MoS₂-PEI composite show typical XRD diffraction peaks at 33°, 44°, and 59° assigned to the (101), (103), and (110) planes of the hexagonal-phase MoS₂ (JCPDS No. 89-5112), respectively. However, the peaks corresponding to (002) plane for the two samples emerge both at lower-angle positions relative to that of the standard MoS₂ (JCPDS No. 89-5112), showing increased interlayer distances of 10.0 and 10.8 Å, respectively (Fig. 2f and inset). In addition, (004) peaks corresponding to half distance of MoS₂ interlayers also appear for the two samples. The increase in *d*-spacing of (002) plane for the pre-intercalated MoS₂ and MoS₂-PEI composite is ascribed to the intercalation of Na⁺/NH₄⁺ and PEI molecules into the MoS₂ interlayers, respectively. However, after the thermal

treatments, the annealed MoS₂ and the MoS₂/NC samples obtained from the pre-intercalated MoS₂ and MoS₂-PEI composite exhibit remarkable difference in final interlayer distance. For the annealed MoS₂, the interlayer distance is reduced to 6.2 Å at ~14° (Fig. 2g), corresponding to the standard value of the normal MoS₂, which indicates that the inserted NH₄⁺ ions in the layers of pre-intercalated MoS₂ were released at a higher temperature over 200 °C^{38,39}. Nevertheless, for the MoS₂/NC hetero-aerogel, the interlayer distance of MoS₂ was reduced to 9.8 Å (Fig. 2g), a value according with that of graphene-inserted MoS₂ nanosheets³⁰, confirming the existence of a graphene-like carbon layer in the interlayers of MoS₂ induced by the in situ carbonization of PEI. Raman spectroscopy tests also confirmed the formation of the MoS₂/NC hetero-aerogel, as shown in Supplementary Fig. 4. It can be seen that Raman spectrum of the annealed MoS₂ shows two distinct peaks at 376.5 and 402.6 cm⁻¹

ascribed to the typical E_{2g}^1 (the in-plane displacement of Mo and S atoms), and A_g^1 vibration modes (out-of-plane symmetric displacement of S atom along the c axis) of MoS_2 . However, for the MoS_2/NC heteroerogel, the two peaks shift to 378.1 and 400.2 cm^{-1} , respectively. The blue shift of E_{2g}^1 peak and the red shift of A_g^1 peak are particular signals induced by the carbon insertion^{40,41}. Besides, the other two peaks centered at ~ 1350.1 and ~ 1590.9 cm^{-1} corresponding to the typical D and G bands of graphitized carbons are also observed. The mass ratio of MoS_2 and carbon components was measured to be 74:26 based on thermal gravimetric analysis (TGA) method (Supplementary Fig. 5), during which carbon was completely removed and MoS_2 was oxidized completely to MoO_3 ^{12,42}. The carbon content (26%) in the heteroerogel is contributed by both the carbon in the interlayers and on the surface of MoS_2 nanosheets.

Influence of content of polyethyleneimine intercalator. The influence of some key factors such as content and molecular weight (Mw) of PEI on the direct-intercalation behavior and the structure of resulted MoS_2/NC composites was investigated. Supplementary Fig. 6 shows XRD patterns of MoS_2 -PEI composites after the intercalation of PEI with different mass percentages of 16.7–50 wt%, and their corresponding MoS_2/NC composites after carbonization. It is noted that the mass percentage of 44.4 wt% is the typical condition for the direct intercalation of PEI and the preparation of the MoS_2/NC heteroerogel that have been discussed above. In Supplementary Fig. 6a, the (002) peaks with an expanded d -spacing of 10.8 Å are observed in the corresponding XRD patterns of all the four samples of MoS_2 -PEI composites, indicating the effective intercalation of PEI molecules with the various contents. After annealing treatments, the d -spacings of (002) peaks for all the samples are reduced, yet to different extents (Supplementary Fig. 6b). The MoS_2/NC sample derived from a higher PEI content (50 wt%) shows a similar (002) plane d -spacing of 9.8 Å to the typical sample (44.4 wt% PEI), indicating the successful insertion of a graphene layer into MoS_2 nanosheets. However, the high PEI content led to the excessive coating of graphitized carbon on the surface of MoS_2 nanosheets after carbonization, which may suppress the peak intensity of MoS_2 , as shown in Supplementary Fig. 6b. For the samples derived from lower PEI contents (33.3 and 16.7 wt%), their corresponding d -spacings of (002) plane are reduced partially or completely to 6.2 Å, the normal d -spacing value of (002) plane of the standard MoS_2 nanosheets. The results demonstrate that small amounts of PEI may be prone to be expelled out from the interlayers of MoS_2 nanosheets in the MoS_2 -PEI composites during the carbonization process at high temperatures. Therefore, sufficient PEI is necessary for the preparation of MoS_2/NC heteroerogel with expended interlayers of MoS_2 nanosheets via the direct-intercalation strategy. Supplementary Fig. 7 shows XRD patterns of MoS_2 -PEI composites and their corresponding MoS_2/NC composites prepared by using PEI with different molecular weights.

Influence of molecular weight and type of polymer intercalators. Interestingly, it is found that PEI with a wide range of molecular weight from 600 to as high as 70,000, can direct intercalate into the interlayers of MoS_2 nanosheets (Supplementary Fig. 7a) and exist stably as graphene layers in the MoS_2 interlayers after carbonization (Supplementary Fig. 7b), leading to the formation of the novel MoS_2/NC composites. The D, G bands are clearly observed for all the samples, indicating the graphitization of the carbon component in the composites (Supplementary Fig. 8). In contrast, the highest peak intensity ratios, 2.21 and 1.38, of (002)/(101) are obtained for the MoS_2 -PEI composite and

its corresponding MoS_2/NC composite derived from the intercalation of PEI (Mw 600), respectively, indicating the best intercalation effect (Supplementary Fig. 7c). Generally speaking, polymers with a higher molecular weight and a longer chain are more difficult to intercalate into interlayers of MoS_2 nanosheets. The realization of direct intercalation of PEI may be attributed to the relatively expended interlayer distance (10 Å) of the pre-intercalated MoS_2 nanosheets and the electrostatic force between the cationic PEI and the negatively charged MoS_2 . To extend the scope of the PDI strategy, polyethylene glycol (PEG) which contains oppositely charged -OH groups was employed and systematically investigated with the influence of its content and molecular weight on the direct intercalation behavior and the formation of $\text{MoS}_2/\text{carbon}$ (MoS_2/C) composites (Supplementary Figs. 9–12). The results indicate that PEG with different molecular weights of 400–20,000 can also serve as an effective intercalator, resulting in a much larger MoS_2 interlayer distance of 15.6 Å for MoS_2 -PEG composites and a similar interlayer distance of 9.8 Å for the MoS_2/C composites after carbonization (Supplementary Fig. 11). The detailed information regarding direct intercalation by PEI and PEG and the finally resulted MoS_2/NC and MoS_2/C products is summarized in Supplementary Tables 1 and 2.

We noted that the sonication applied in the intercalation process can cause the degradation of polymers, forming lower molecular weight polymers^{43–45} or even small molecules such as oligomers that may intercalate into interlayers of MoS_2 and result in interlayer expansion. To confirm the intercalation effect is contributed by polymers rather than oligomers generated during sonication of polymers, systematic experiments and measurements using gel permeation chromatography (GPC) and liquid chromatography-mass spectrometry (LC-MS) were conducted (Supplementary Figs. 13–16 and Supplementary Tables 3, 4).

Molecular dynamics calculations. The intercalation of 2D layered materials by using ions or small molecule (Li^+ , Na^+ , NH_4^+ , glucose, etc.) has been well studied^{13,23–27}. However, the direct intercalation by polymers has been rarely reported. To explore the configurations of polymer-intercalated MoS_2 molecular layers and understand how polymers diffused into MoS_2 interlayers, ab initio molecular dynamics (AIMD) calculations were performed (Supplementary Note 2). Figure 3a, b shows the configurations of PEI-intercalated MoS_2 with a interlayer distance of 10.8 Å, where a 3D periodic boundary box of $26.58 \times 26.58 \times 14$ Å³ is adopted. The calculation results reveal that, 5 PEI molecules together with 18 H_2O molecules and 17 NH_4^+ ions arranging in an initial ordered state and a final relaxed state between the two adjacent monolayers of MoS_2 nanosheets can both give an interlayer distance of 10.8 Å, agreeing with the experimental value. Similarly, two different configurations with a selected periodic boundary box of $26.58 \times 26.58 \times 19$ Å³ containing 5 PEG molecules, 18 H_2O molecules, and 17 NH_4^+ ions are illustrated for PEG-intercalated MoS_2 , showing a calculated interlayer distance of 15.6 Å (Supplementary Fig. 17a, b).

We further performed AIMD to simulate the diffusion process of the polymers intercalating into MoS_2 interlayers. The simulation was carried out in a periodic boundary box of $23.06 \times 40.48 \times 13.22$ Å³. In the Y direction, about 20 Å vacuum is added to simulate the edge of MoS_2 . The interlayer distance of MoS_2 nanosheets is about 10 Å, which is close to our experiment measurement. As shown in Fig. 3c–f and Supplementary Movie 1, a PEI molecule is initially placed outside near the MoS_2 layers (Fig. 3c, 0 ps). Then, the NH_2 group in the PEI molecule is attached to the sulfur site on the MoS_2 edge (Fig. 3d, 4 ps). From 6 ps on, the molecule starts to intercalate into MoS_2 layers

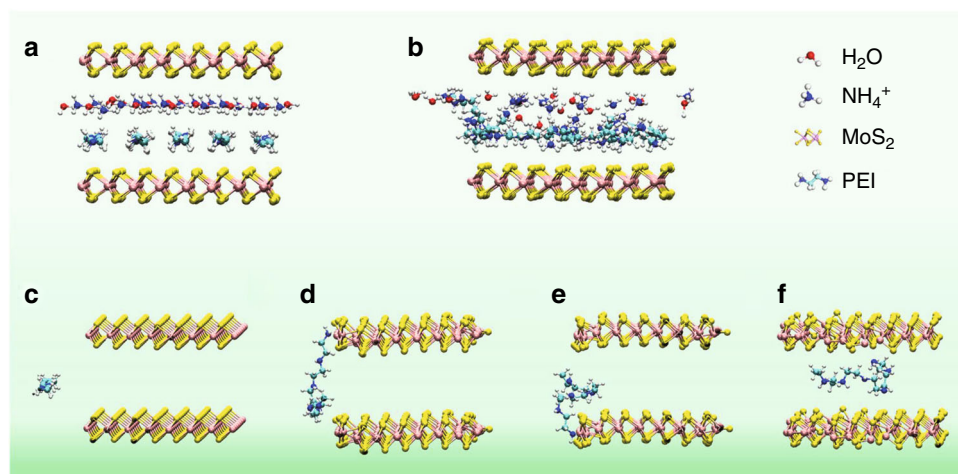


Fig. 3 Molecular dynamics calculations. **a, b** Schematic illustration shows configurations of PEI-intercalated MoS₂ with the resulted interlayer distance of 10.8 Å: **a** an initial ordered state; **b** the final relaxed state. **c–f** Illustration of PEI molecule intercalation process with the MoS₂ interlayer distance of 10 Å: **c** 0 ps, **d** 4 ps, **e** 6 ps, **f** 7 ps

(Fig. 3e). Eventually, the PEI molecule fully enters the interlayer (Fig. 3d, 7 ps). Similarly, for the PEG case, due to the interaction of the OH group and the edge of MoS₂, the molecule first attaches with edge, then the molecule gradually enters the interlayers of MoS₂ (Supplementary Fig. 17c–f and Supplementary Movie 2). The intercalation process of the polymers consists of two steps: the first is the interaction between polymer molecules and the edge of MoS₂ which shorten the distance between the polymer and MoS₂. And the second, the interaction of the polymer molecule with the MoS₂ attracts the molecule entering the interlayer. From our static calculations, the binding energy (BE) of a single molecule of PEG and PEI with MoS₂ is about -1.53 and -1.76 eV, respectively.

It is noted that, the equilibrium interlayer distances induced by the intercalation of PEI and PEG are different (10.8 Å for PEI and 15.6 Å for PEG). We think such difference is attributed to the difference in BE of PEI and PEG to MoS₂ surfaces and the different behaviors of the two polymers in the water environment. First, PEI has a higher BE than PEG to MoS₂ surfaces with a stronger interaction, leading to a closer distance between PEI and MoS₂ layers. Second, the further AIMD simulation indicates that PEI molecules are surrounded by less H₂O molecules and have a smaller first solvation shell (2.62 Å) than that of PEG (2.75 Å) in aqueous solution (Supplementary Fig. 18). The average distance between PEI molecules and their solvation shell is slightly smaller, which gives rise to a smaller interlayer distance of MoS₂ nanosheets.

Electrochemical performance. The electrochemical performance of the MoS₂-based hetero aerogels as electrodes of supercapacitors was measured in a three-electrode cell in the presence of 6.0 M KOH solution. Figure 4a shows representative cyclic voltammetry (CV) curves of the MoS₂/NC and MoS₂/C hetero aerogels as well as the annealed MoS₂ nanosheets at a sweep rate of 5 mV s⁻¹ in the potential range of -0.2 to 0.6 V. The CV curves for all three electrodes display pairs of redox peaks, proving the presence of a reversible Faradic reaction and PC behavior between different valence states of Mo ions (+2 to +6). The peak intensity and curve area for pure MoS₂ are pretty low (the inset of Fig. 4a), indicating that the capacitance of pure MoS₂ is negligible. With increasing the scanning rate, the curve shapes for MoS₂-based hetero aerogels are basically preserved (Supplementary Fig. 19a–c), suggesting fast and stable reversible reactions over the composite electrodes. Figure 4b shows the galvanostatic charge/

discharge curves of the three electrodes at 1 A g⁻¹, where several sloping plateaus are observed, in good agreement with the CV results. Obviously, the voltage plateaus for the MoS₂/C and MoS₂/NC hetero aerogel electrodes, especially the latter, are much more pronounced during both the charging and discharging processes, suggesting a significantly enhanced PC energy storage relative to pure MoS₂.

An ultrahigh specific capacitance of 4144 F g⁻¹ is obtained for the MoS₂/NC hetero aerogel electrode at a current density 1 A g⁻¹, which is much higher than those of the MoS₂/C hetero aerogel (2576 F g⁻¹) and the pure annealed MoS₂ (259 F g⁻¹). This value of specific capacitance also far surpasses those of previously reported high-capacitance electrodes based on metal sulfides, phosphides and oxides, such as NiS nanoframes (2112 F g⁻¹ at 1 A g⁻¹)⁴⁶, MnCo₂S₄ hollow tubular structures (1203 F g⁻¹ at 2 A g⁻¹)⁴⁷, NiCo₂S₄ nanosheets (1231 F g⁻¹ at 2 A g⁻¹)⁴⁸, Ni₂P nanosheets arrays (3496 F g⁻¹ at 2.5 A g⁻¹)⁴⁹, NiO atomic clusters/graphene (3023 F g⁻¹ at 1 A g⁻¹)⁵⁰, and amorphous Ni(OH)₂ (3262 F g⁻¹ at 5 mV s⁻¹), etc⁵¹. The ultrahigh capacitance of the MoS₂/NC hetero aerogel should be resulted from its synergistic effect in structure and composition, because the capacitance contributed from the annealed pristine MoS₂ (Fig. 4a), N-containing carbon (NC) by direct carbonization of PEI and blank electrode of pristine Ni foam (Supplementary Fig. 20) is almost negligible at the same current density. Moreover, the MoS₂/NC hetero aerogel electrode exhibits higher capacitances of 3550, 3150, 2900, 2670, and 2483 F g⁻¹ at current densities of 2, 4, 6, 8, and 10 A g⁻¹ than the other two electrodes, respectively, demonstrating an excellent rate capability (Fig. 4c and Supplementary Fig. 19d–f). The MoS₂/NC hetero aerogel electrode also demonstrates remarkable long-term cycling stability. As shown in Fig. 4d, the electrode shows only an ~8% capacitance decrease after an 8000-cycle charge/discharge test at 10 A g⁻¹. The quasi-triangular shape of the discharge/charge curves is still well preserved in the last 5 cycles, indicating the hetero aerogel electrode is stable during the long-term cycling. Such outstanding combined capacitance-rate performances thanks to the PDI strategy which creates efficient pathways for electrons/ions transport and provides more active sites for reversible redox reactions.

Electrochemical reactions kinetics analysis. As can also be seen in the Nyquist plots, the contact resistance (R_s) and charge transfer resistance (R_{ct}) of the MoS₂/NC hetero aerogel electrode

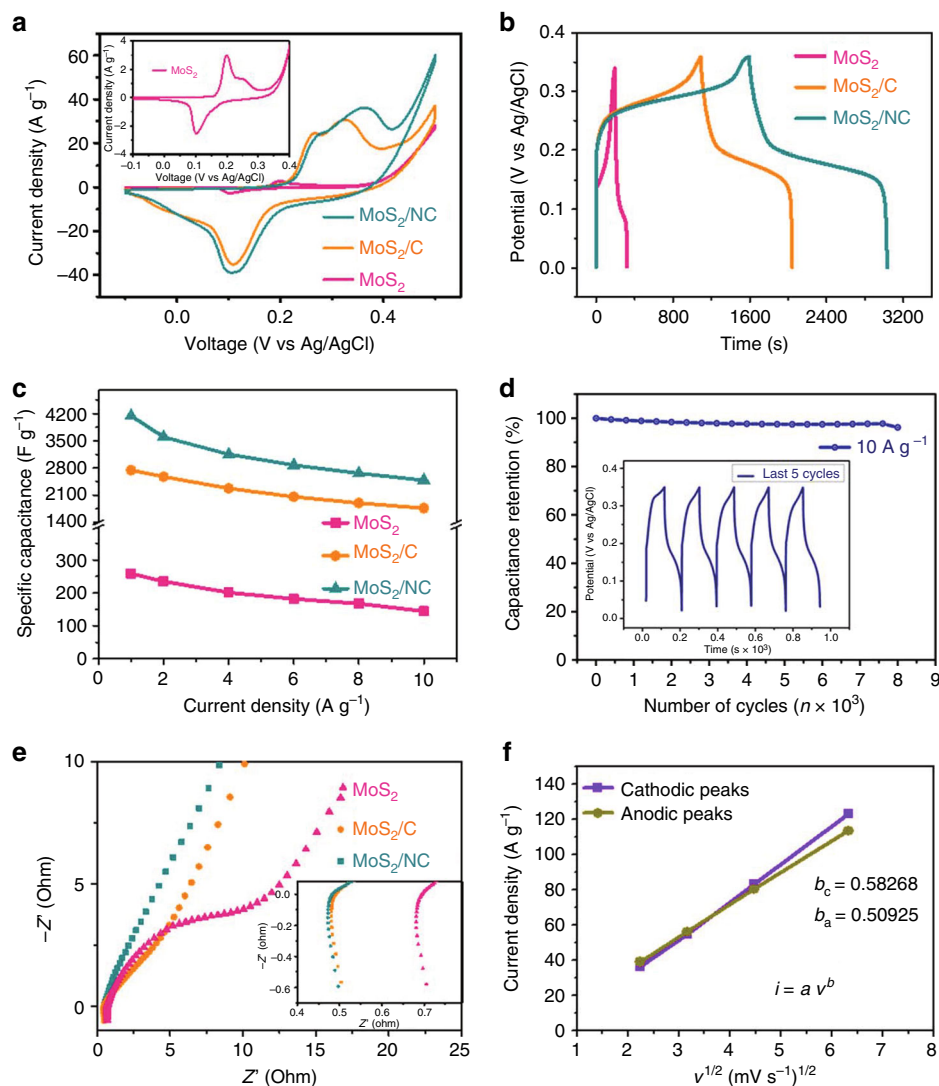


Fig. 4 Electrochemical performance. **a–c** CV curves at 5 mV s^{-1} (**a**), galvanostatic charging–discharging curves at 1 A g^{-1} (**b**), and specific capacitances at different current densities from 1 to 10 A g^{-1} (**c**) of MoS_2 nanosheets, and the MoS_2/C and MoS_2/NC heteroaggregates. **d** Cycling performance at a current density of 10 A g^{-1} of the MoS_2/NC heteroaggregates. The inset in (**d**) shows charging–discharging curves of the last 5 cycles. **e** Nyquist plots of the three electrodes. **f** Dependence of the peak current density on square root of sweep rate of the MoS_2/NC heteroaggregates

are both the lowest among the three electrodes (Fig. 4e and the inset), suggesting the excellent conductivity and compatible electrode–electrolyte interface. The Nyquist plots demonstrated a conspicuously decreased R_{ct} for the MoS_2 -based heteroaggregates, compared with the pure MoS_2 . The enhanced capability of charge transfer should be ascribed to the graphitized carbon inserting into MoS_2 interlayers and coating on the surfaces of MoS_2 nanosheets, which ensures the effective electron transfer between nanosheets in the composite heteroaggregates during capacitive process.

Kinetics analysis of the MoS_2/NC heteroaggregates electrode was conducted based on their CV curves shown in Supplementary Fig. 19a. From the plots of peak current density (I_p) versus square root of sweep rate ($v^{1/2}$) from 2 to 40 mV s^{-1} for both cathodic and anodic peaks (Fig. 4f), the current follows well a power-law relationship with the sweep rate ($I_p = a v^b$). A b -value of 0.5 indicates that the current is controlled by semi-infinite linear diffusion, whereas a value of 1 indicates that the current is surface-controlled. Specifically, the b -value was calculated to be ~ 0.58 and ~ 0.51 from the cathodic peak and anodic peak, respectively. The result indicates that the electrode kinetics under

the conditions investigated was both diffusion- and surface-controlled, demonstrating a combined PC energy storage contributed from battery-like ion intercalation reactions and fast surface redox reactions. Since the b -values are closer to 0.5, the diffusion-controlled ion intercalation effect may be predominant in the whole PC energy storage process, which is facilitated by interlayer distance expansion of the MoS_2/NC heteroaggregates that allows efficient ion diffusion into/from the interlayers.

X-ray photoelectron spectroscopy analyses. In order to probe the interfacial interactions between MoS_2 and carbon-based (C or NC) components, X-ray photoelectron spectroscopy (XPS) examination was conducted for the MoS_2 -based heteroaggregates and the annealed pristine MoS_2 . A survey XPS spectrum of the MoS_2/NC heteroaggregates provides direct evidence of the presence of C, N, Mo, and S in the heteroaggregates (Supplementary Fig. 21). The C 1s spectrum of MoS_2/NC heteroaggregates exhibits a strong and sharp peak of C–C (284.6 eV) with the weak peaks of C–N (285.5 eV) and C=N (287.0 eV), implying that the graphite carbon is the majority species (Fig. 5a). The two prominent peaks of

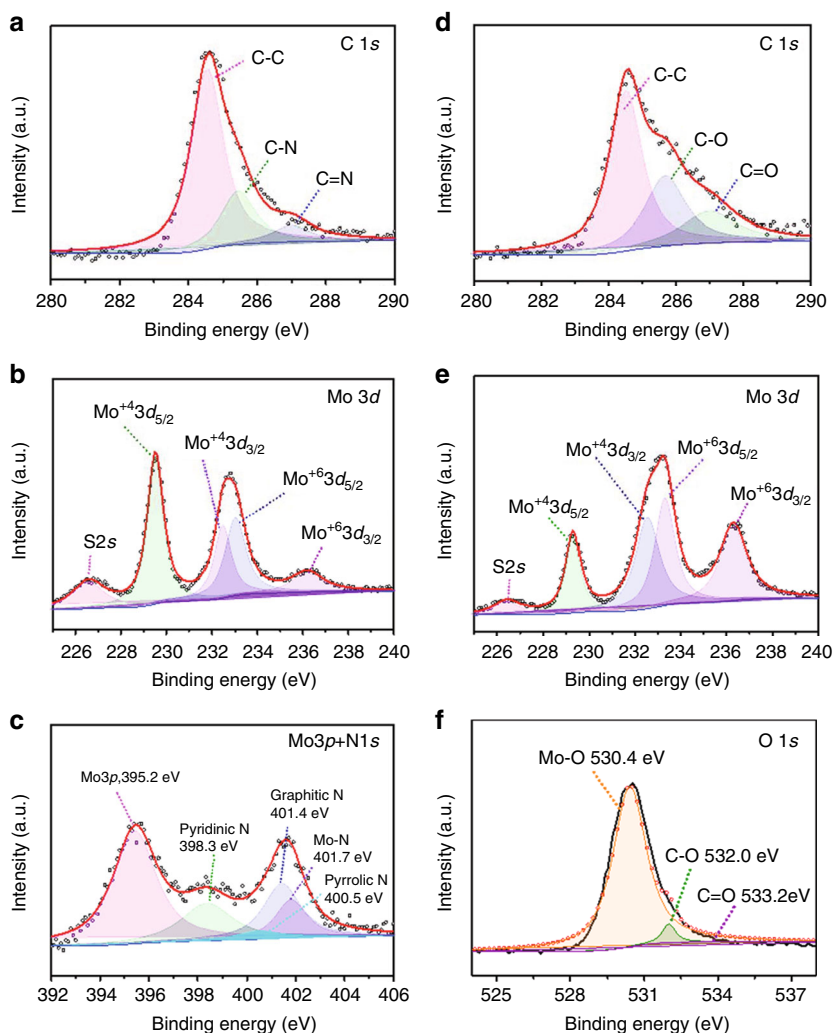


Fig. 5 X-ray photoelectron spectroscopy analyses. **a–c** High-resolution XPS spectra of C 1s (**a**), Mo 3d (**b**), and Mo 3p + N 1s (**c**) of the MoS₂/NC hetero-aerogels. **d–f** High-resolution XPS spectra of C 1s (**d**), Mo 3d (**e**), and O 1s (**f**) of the MoS₂/C hetero-aerogels

S $2p_{1/2}$ at 163.2 eV and S $2p_{3/2}$ at 162.2 eV in the core-level S $2p$ XPS spectrum are assigned to the S²⁻ in MoS₂ of the hetero-aerogel (Supplementary Fig. 22), similar to those of the pristine MoS₂ (Supplementary Fig. 23a). The high-resolution Mo 3d XPS of the MoS₂/NC hetero-aerogel reveals that the BEs of Mo $3d_{3/2}$ at 232.4 eV and Mo $3d_{5/2}$ at 229.5 eV are related to the Mo⁴⁺ ion in the pristine MoS₂ (Fig. 5b). Notably, compared with pure MoS₂ (Supplementary Fig. 23b) a new peak at 236.2 eV and a deconvoluted peak at 233.0 eV emerge in the XPS spectrum of Mo 3d for the MoS₂/NC hetero-aerogel, corresponding to Mo⁶⁺ $3d_{5/2}$ and $3d_{3/2}$ respectively (Fig. 5b). The deconvolution of N 1s energy level signals for the MoS₂/NC hetero-aerogel reveals the peaks at 398.3, 400.5, and 401.4 eV, which are assigned to pyridinic, pyrrolic, and graphitic N (Fig. 5c), respectively. Although the N 1s and Mo 3p spectra are partially overlapped, a distinct N 1s peak can still be observed at 401.7 eV, assigned to the coordination interactions between the MoS₂ nanosheets and the N species in the carbon^{52,53}. Accordingly, the valence increase of Mo ions is considered as a result of electron transfer from NC component to MoS₂ via interfacial chemical bonds, i.e., Mo–N bonds between the two components, as evidenced by the Mo 3p + N 1s XPS spectrum in Fig. 5c. For the MoS₂/C hetero-aerogel, in addition to typical C–C bonds as the majority, C–O and C=O bonds derived from PEG intercalator is found existing in the hetero-aerogel (Fig. 5d). Interestingly, Mo⁶⁺ ions are also present, which may be

induced by similar electron transfer from Mo to O atoms via interfacial Mo–O bonds between MoS₂ and carbon components in the composite (Fig. 5e, f)⁵⁴. The strong interactions between MoS₂ and carbon-based components via the Mo–N or Mo–O bonds can distort the intrinsic Mo–S bonds of MoS₂, thus leading to a disordered crystal lattice arrangement, as mirrored in Fig. 2b. The above results demonstrate that MoS₂ nanosheets in the two composites are chemically bonded with the carbon-based components via Mo–N or Mo–O bonds, with increased valence of central Mo ions and efficient across-nanosheet electron transfer pathways through the interfacial bonds.

Discussion

Taking all into account, we think the superior PC performance of the MoS₂-based hetero-aerogels, especially the MoS₂/NC hetero-aerogel, is ascribed to their intriguing structural/composition advantages induced by the PDI behavior. First, the 3D hetero-aerogels made of the stably stacked MoS₂ framework and interconnected graphitized carbon network, derived from PEI adsorption on the surface of MoS₂ nanosheets, offer stable ions diffusion channels and fast electron transport between MoS₂ nanosheets (Fig. 6a), compared with that of pure MoS₂ powder (Fig. 6b). Second, expanded interlayers of MoS₂ nanosheets by the insertion of a graphene-like carbon monolayer derived from PDI

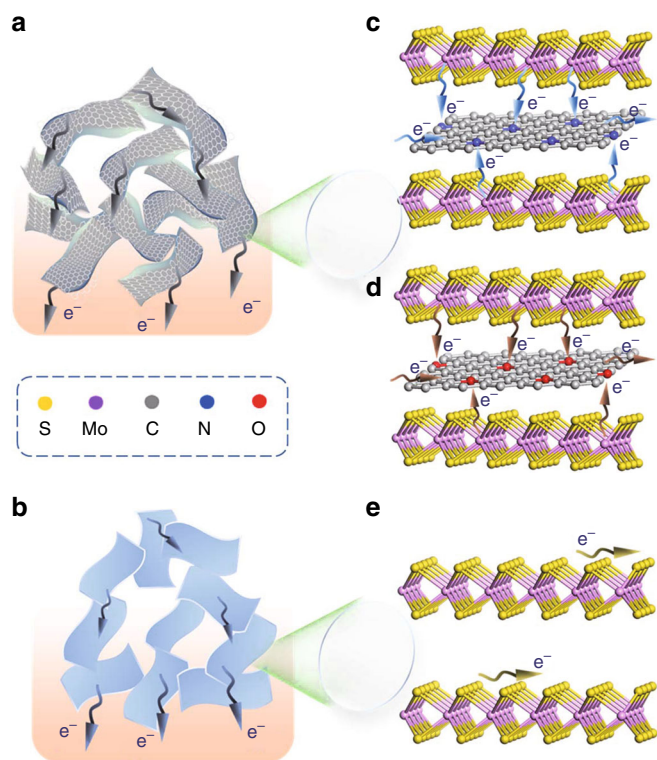


Fig. 6 Schematic illustration of different electron transport pathways. **a, b** Electron transport pathways between MoS₂ nanosheets in the MoS₂-based hetero-aerogels (**a**) and pure MoS₂ powder (**b**). **c, d** Electron transport pathways across MoS₂ monolayers in the MoS₂/NC hetero-aerogel (**c**) and MoS₂/C hetero-aerogel (**d**). **e** Electron transport pathways within MoS₂ monolayers in pure MoS₂ powder

expose more accessible active sites for redox reactions and create new pathways for ion/electron transport (Fig. 6c, d), which makes each monolayer of MoS₂ electrochemically active. For pure MoS₂, with unexpanded intrinsic interlayers and poor conductivity, electron transfer along the pathways within (002) plane illustrated in Fig. 6e may be very inefficient. In particular, for the MoS₂/NC hetero-aerogel, electron transfer through metallic bond-like interfacial Mo–N bonds within the hetero-aerogel is more efficient than that via covalent bond-like Mo–O bonds within the MoS₂/C hetero-aerogel (Fig. 6c, d)⁵⁵. As a consequence, the MoS₂/NC hetero-aerogel electrode demonstrates unprecedented PC energy storage performance.

In summary, the PDI strategy has been proposed for the preparation of interlayer-expanded MoS₂ nanosheets and MoS₂/carbon hetero-aerogels for ultrahigh-capacitance supercapacitors. The strategy is facile, mild, and efficient, which is applicable to differently charged polymers with a wide range of molecular weight. The direct intercalation behavior of polymers has been investigated systematically by substantial characterizations and molecular dynamic calculations. The resulting MoS₂/carbon hetero-aerogels exhibited outstanding supercapacitor performance such as ultrahigh capacitance, remarkable rate capability, and excellent cycling stability. The superior performance is attributed to the structural and composition advantages of the unique MoS₂/carbon hetero-aerogels with a 3D conductive MoS₂/C framework, expanded interlayers of MoS₂ nanosheets, interoverlapped MoS₂/C layered heterointerface as well as a high content of MoS₂ (up to 74%) and a high valence (+6) of central Mo ions, which are conducive to not only fast and stable charge transfer/diffusion, but also enhanced ions intercalation pseudocapacitance. The

novel PDI strategy may be generally applicable to other 2D layered materials. This study may offer an opportunity for the development of 2D materials-based composites with desirable structure and property for promising energy applications.

Methods

Synthesis of pre-intercalated pristine MoS₂ nanosheets. All the reagents mentioned in the experiment were purchased from Aladdin Biological Technology Co., LTD (China) and used without further purification. The pre-intercalated MoS₂ nanosheets were synthesized through a simple hydrothermal method. In a typical procedure, sodium molybdate (Na₂MoO₄, 0.3 g) and thioacetamide (TAA, C₂H₅NS, 0.6 g) were dissolved in DI water (20 mL) mixed with ethylene glycol (10 mL) under continuous stirring for 30 min to form a homogeneous solution. Then, the mixture was transferred into a 100 mL Teflon-lined stainless-steel autoclave, and hydrothermally treated at 220 °C for 24 h. After naturally cooled to room temperature, the resulting black precipitate of pre-intercalated MoS₂ was collected by filtration and washed with distilled water for several times to remove the residue of reactants. Finally, the obtained MoS₂ black product was calcined at 300 °C in the flowing argon for 2 h at a heating rate of 2 °C min⁻¹ and marked as the annealed pristine MoS₂.

Synthesis of MoS₂/NC and MoS₂/C hetero-aerogels. In a typical synthesis of MoS₂/NC hetero-aerogel, 1.6 g PEI (Mw = 600, Aladdin) and 2.0 g MoS₂ with a mass ratio of 44 wt% were mixed in a certain amount of water under sonication for 1 h to form a suspension, followed by freeze-drying treatment, resulting in a MoS₂-PEI composite. Then, the obtained MoS₂-PEI composite was annealed at 800 °C for 6 h with argon flow, leading to a black product of the MoS₂/NC hetero-aerogel. For the synthesis of MoS₂/C hetero-aerogel, typically, the polymer of PEG (Mw = 400) was employed instead of PEI under otherwise the same conditions. The final composite hetero-aerogels prepared by using PEI (Mw = 600) and PEG (Mw = 400) were regarded as the standard samples and were denoted as MoS₂/NC and MoS₂/C, respectively. The mass percentage of polymers employed for direct intercalation was 44 wt% if not specified.

Characterizations. The crystal structure of the samples was characterized by XRD using a D/max2550VB3+/PC X-ray diffractometer with Cu K α radiation ($\lambda = 0.15418$ nm) at 40 kV, 100 mA. The 2θ degree range used in the measurements was from 5° to 80°. The morphology was observed using a SEM (Hitachi S4800, 3 kV) equipped with an EDS analysis system and a HRTEM (JEM 2011, 200 kV). XPS investigation was conducted in a PHI-5000C ESCA system (PerkinElmer) with Mg K α radiation ($h\nu = 1253.6$ eV). The XPS spectra were measured with a constant analyzer pass energy of 46.95 eV. All BEs were referred to the C 1s peak (284.6 eV) arising from surface hydrocarbons (or adventitious hydrocarbon). Raman spectra were recorded by using a spectrophotometer (inVia, Renishaw, Germany) with a 514 nm laser. Thermogravimetric analysis (NETZSCH STA409PC) was carried out from 25 to 700 °C at a heating rate of 10 °C min⁻¹ under flowing air. A zeta potential instrument (zetasizer Nano Z) was used for determining the surface charge of the MoS₂/NC hetero-aerogel samples. The specific surface area was measured by the multipoint Brunauer–Emmett–Teller (BET) method at 77.3 K with a Quantachrome NOVA-4200e system. Molecular weight distribution of polymers was studied with GPC using a system from Agilent Technologies 1100. Samples were dissolved in H₂O. For the measurement, 20 μ L of sample was injected. The chromatography was performed at 40 °C using 0.1 mol/L NaNO₃ as eluent with a flow rate of 0.5 mL/min. Mass spectra were measured on a LC-MS Varian 310 instrument.

Fabrication and electrochemical test of supercapacitors. All the electrochemical measurements were conducted on a standard three-electrode setup in an electrochemical cell by using a CHI 660E electrochemical workstation (CH Instruments, Inc., Shanghai) in an aqueous KOH electrolyte (6.0 M), where a Pt wire and a saturated Ag/AgCl electrode (filled with saturated KCl with a potential of 0.197 V versus SHE) serve as the counter electrode and the reference electrode, respectively. The working electrode was prepared by mixing active materials, conductive carbon black (Super-P), and polymer binder (polytetrafluoroethylene, PTFE) in a weight ratio of 8:1:1. The mixture was pressed onto a Ni foam that was first treated with a 5% HCl solution, and then was dried at 100 °C for 24 h under vacuum to remove the solvent. The working area of the electrode was set as 1 \times 1 cm² and the mass loading of the electrode materials was controlled to be around 2.5 mg. In addition, before each electrochemical test, the electrode was immersed into the electrolyte for 4–5 h.

Cyclic voltammograms (CV), galvanostatic charge/discharge (GCD), and electrochemical impedance spectroscopy (EIS), measurements were performed by using a CHI 660E workstation at ambient temperature. The CVs were recorded from -0.2 to 0.6 V at scan rates of 5–80 mV s⁻¹. The GCD measurements were performed at the current densities of 1–40 A g⁻¹ with cutoff voltage of 0–0.37 V. EIS was recorded by applying the open-circuit potential with an amplitude of 5 mV over the frequency range from 100 kHz to 0.01 Hz. All potential values for electrochemical measurements were calibrated to the Ag/AgCl reference electrode.

Cyclic stability was characterized using galvanostatic charge–discharge measurements over 8000 cycles at a charge–discharge rate of 10 A g^{-1} . The specific capacitances of the electrodes are calculated using the following equation⁵⁶:

$$C = \frac{2i_m \int V_i dt}{V_i^2} \quad (1)$$

where C (F g^{-1}) is the specific capacitance, $i_m = I/m$ (A g^{-1}) is the current density, where I represents the current and m represents the active mass of the electrode. $\int V_i dt$ represents the integral current area and V represents the potential with initial and final values of V_i and V_f respectively.

Data availability

The data that support the findings of this study are available within the paper and its Supplementary Information file, or from the corresponding author on request.

Received: 31 July 2018 Accepted: 21 February 2019

Published online: 26 March 2019

References

- Patrice, S. & Yury, G. Materials for electrochemical capacitors. *Nat. Mater.* **7**, 845–854 (2008).
- Chhowalla, M. et al. The chemistry of two-dimensional layered transition metal dichalcogenide nanosheets. *Nat. Chem.* **5**, 263–275 (2013).
- Feng, J. et al. Metallic few-layered VS_2 ultrathin nanosheets: high two-dimensional conductivity for in-plane supercapacitors. *J. Am. Chem. Soc.* **133**, 17832–17838 (2011).
- Ma, G. et al. In situ intercalative polymerization of pyrrole in graphene analogue of MoS_2 as advanced electrode material in supercapacitor. *J. Power Sources* **229**, 72–78 (2013).
- Acerce, M., Voiry, D. & Chhowalla, M. Metallic 1 T phase MoS_2 nanosheets as supercapacitor electrode materials. *Nat. Nanotechnol.* **10**, 313–318 (2015).
- Rapoport, L., Fleischer, N. & Tenne, R. Applications of WS_2 (MoS_2) inorganic nanotubes and fullerene-like nanoparticles for solid lubrication and for structural nanocomposites. *J. Mater. Chem.* **15**, 1782–1788 (2005).
- Stephenson, T., Li, Z., Olsen, B. & Mitlin, D. Lithium ion battery applications of molybdenum disulfide (MoS_2) nanocomposites. *Energy Environ. Sci.* **7**, 209–231 (2014).
- Xiao, J. et al. Electrochemically induced high capacity displacement reaction of $\text{PEO}/\text{MoS}_2/\text{graphene}$ nanocomposites with lithium. *Adv. Funct. Mater.* **21**, 2840–2846 (2011).
- Ji, H. et al. Porous hybrid composites of few-layer MoS_2 nanosheets embedded in a carbon matrix with an excellent supercapacitor electrode performance. *Small* **11**, 6480–6490 (2015).
- Kong, D. et al. Rational design of $\text{MoS}_2/\text{graphene}$ nanocables: towards high performance electrode materials for lithium ion batteries. *Energy Environ. Sci.* **7**, 3320–3325 (2014).
- Qiu, W., Jiao, J., Xia, J., Zhong, H. & Chen, L. Phosphorus-doped graphene-wrapped molybdenum disulfide hollow spheres as anode material for lithium-ion batteries. *RSC Adv.* **4**, 50529–50535 (2014).
- Teng, Y. et al. MoS_2 nanosheets vertically grown on graphene sheets for lithium-ion battery anodes. *ACS Nano* **10**, 8526–8535 (2016).
- Zhao, C. et al. Self-assembly-induced alternately stacked single-layer MoS_2 and N-doped graphene: a novel van der Waals heterostructure for lithium-ion batteries. *ACS Appl. Mater. Interfaces* **8**, 2372–2379 (2016).
- Ding, S., Chen, J. S. & Lou, X. W. Glucose-assisted growth of MoS_2 nanosheets on CNT backbone for improved lithium storage properties. *Chemistry* **17**, 13142–13145 (2011).
- Chen, W.-X., Ma, L., Xu, Z.-D., Xia, J.-B. & Li, X. Carbon nanotubes coated with tubular MoS_2 layers prepared by hydrothermal reaction. *Nanotechnology* **17**, 571–574 (2006).
- Shi, Y. et al. Self-assembly of hierarchical MoS_2/CNT nanocomposites ($2 < x < 3$): towards high performance anode materials for lithium ion batteries. *Sci. Rep.* **3**, 2169–2077 (2013).
- Wang, S. et al. Solvothermal synthesis of $\text{MoS}_2/\text{carbon}$ nanotube composites with improved electrochemical performance for lithium ion batteries. *Nanosci. Nanotechnol. Lett.* **4**, 378–383 (2012).
- Hu, L., Ren, Y., Yang, H. & Xu, Q. Fabrication of 3D hierarchical $\text{MoS}_2/\text{polyaniline}$ and MoS_2/C architectures for lithium-ion battery applications. *ACS Appl. Mater. Interfaces* **6**, 14644–14652 (2014).
- Yang, L. et al. Hierarchical $\text{MoS}_2/\text{polyaniline}$ nanowires with excellent electrochemical performance for lithium-ion batteries. *Adv. Mater.* **25**, 1180–1184 (2013).
- Zhang, C., Wang, Z., Guo, Z. & Lou, X. W. Synthesis of $\text{MoS}_2\text{-C}$ one-dimensional nanostructures with improved lithium storage properties. *ACS Appl. Mater. Interfaces* **4**, 3765–3768 (2012).
- Xu, J., Zhang, J., Zhang, W. & Lee, C. S. Interlayer nanoarchitectonics of two-dimensional transition-metal dichalcogenides nanosheets. *Adv. Energy Mater.* **7**, 1700571 (2017).
- Rasamani, K. D., Alimohammadi, F. & Sun, Y. Interlayer-expanded MoS_2 . *Mater. Today* **20**, 83–91 (2017).
- Anto Jeffery, A., Nethravathi, C. & Rajamathi, M. Two-dimensional nanosheets and layered hybrids of MoS_2 and WS_2 through exfoliation of ammoniated MS_2 ($M = \text{Mo}, \text{W}$). *J. Phys. Chem. C* **118**, 1386–1396 (2014).
- Li, Y. et al. Enhancing sodium-ion battery performance with interlayer-expanded $\text{MoS}_2\text{-PEO}$ nanocomposites. *Nano Energy* **15**, 453–461 (2015).
- Liang, Y. et al. Interlayer-expanded molybdenum disulfide nanocomposites for electrochemical magnesium storage. *Nano Lett.* **15**, 2194–2202 (2015).
- Somoano, R. B., Hadek, V. & Rembaum, A. Alkali metal intercalates of molybdenum disulfide. *J. Chem. Phys.* **58**, 697–701 (1973).
- Zheng, J. et al. High yield exfoliation of two-dimensional chalcogenides using sodium naphthalenide. *Nat. Commun.* **5**, 2995–3003 (2014).
- Chang, K. et al. Graphene-like $\text{MoS}_2/\text{amorphous carbon}$ composites with high capacity and excellent stability as anode materials for lithium ion batteries. *J. Mater. Chem. C* **21**, 6251–6259 (2011).
- Gao, M. R., Chan, M. K. & Sun, Y. Edge-terminated molybdenum disulfide with a 9.4 \AA interlayer spacing for electrochemical hydrogen production. *Nat. Commun.* **6**, 7493–7500 (2015).
- Jiang, H. et al. 2D monolayer $\text{MoS}_2\text{-carbon}$ interoverlapped superstructure: engineering ideal atomic interface for lithium ion storage. *Adv. Mater.* **27**, 3687–3695 (2015).
- Liu, N. et al. Microwave-assisted reactant-protecting strategy toward efficient MoS_2 electrocatalysts in hydrogen evolution reaction. *ACS Appl. Mater. Interfaces* **7**, 23741–23749 (2015).
- Liu, Q. et al. Gram-scale aqueous synthesis of stable few-layered 1 T- MoS_2 : applications for visible-light-driven photocatalytic hydrogen evolution. *Small* **11**, 5556–5564 (2015).
- Wang, X., Guan, Z., Li, Y., Wang, Z. & Chen, L. Guest–host interactions and their impacts on structure and performance of nano- MoS_2 . *Nanoscale* **7**, 637–641 (2015).
- Xie, J. et al. Controllable disorder engineering in oxygen-incorporated MoS_2 ultrathin nanosheets for efficient hydrogen evolution. *J. Am. Chem. Soc.* **135**, 17881–17888 (2013).
- Zhao, X., Hu, C. & Cao, M. Three-dimensional MoS_2 hierarchical nanoarchitectures anchored into a carbon layer as graphene analogues with improved lithium ion storage performance. *Chem. Asian J.* **8**, 2701–2707 (2013).
- Bi, H., Chen, I. W., Lin, T. & Huang, F. A new tubular graphene form of a tetrahedrally connected cellular structure. *Adv. Mater.* **27**, 5943–5949 (2015).
- Wang, P. P., Sun, H., Ji, Y., Li, W. & Wang, X. Three-dimensional assembly of single-layered MoS_2 . *Adv. Mater.* **26**, 964–969 (2014).
- Tang, Y. J. et al. Molybdenum disulfide/nitrogen-doped reduced graphene oxide nanocomposite with enlarged interlayer spacing for electrocatalytic hydrogen evolution. *Adv. Energy Mater.* **6**, 1600116 (2016).
- Xu, Y. et al. Monolayer MoS_2 with S vacancies from interlayer spacing expanded counterparts for highly efficient electrochemical hydrogen production. *J. Mater. Chem. A* **4**, 16524–16530 (2016).
- Chen, J., Xia, Y. & Yang, J. Graphene/surfactant-assisted synthesis of edge-terminated molybdenum disulfide with enlarged interlayer spacing. *Mater. Lett.* **210**, 248–251 (2018).
- Wang, Z. et al. CTAB-assisted synthesis of single-layer $\text{MoS}_2\text{-graphene}$ composites as anode materials of Li-ion batteries. *J. Mater. Chem. A* **1**, 2202–2210 (2013).
- Xu, X. et al. A nanosheets-on-channel architecture constructed from MoS_2 and CMK-3 for high-capacity and long-cycle-life lithium storage. *Adv. Energy Mater.* **4**, 1400902 (2014).
- Watanabe, T. et al. Determination of primary bond scissions by mass spectrometric analysis of ultrasonic degradation products of poly(ethylene oxide-block-propylene oxide) copolymers. *J. Mass Spectrom.* **45**, 799–805 (2010).
- Vijayalakshmi, S. P. & Madras, G. Effect of initial molecular weight and solvents on the ultrasonic degradation of poly(ethylene oxide). *Polym. Degrad. Stab.* **90**, 116–122 (2005).
- Taghizadeh, M. T. & Asadpour, T. Effect of molecular weight on the ultrasonic degradation of poly(vinyl-pyrrolidone). *Ultrason. Sonochem.* **16**, 280–286 (2009).
- Yu, X. Y., Yu, L., Wu, H. B. & Lou, X. W. Formation of nickel sulfide nanoframes from metal–organic frameworks with enhanced pseudocapacitive and electrocatalytic properties. *Angew. Chem.* **54**, 5331–5335 (2015).
- Chen, Y. M., Li, Z. & Lou, X. W. General formation of $\text{M}_x\text{Co}_{(3-x)}\text{S}_4$ ($M = \text{Ni}, \text{Mn}, \text{Zn}$) hollow tubular structures for hybrid supercapacitors. *Angew. Chem.* **54**, 10521–10524 (2015).
- Shen, L. et al. NiCo_2S_4 nanosheets grown on nitrogen-doped carbon foams as an advanced electrode for supercapacitors. *Adv. Energy Mater.* **5**, 1400977 (2015).

49. Zhou, K. et al. Ultrahigh-performance pseudocapacitor electrodes based on transition metal phosphide nanosheets array via phosphorization: a general and effective approach. *Adv. Funct. Mater.* **25**, 7530–7538 (2015).
50. Jeong, H. M. et al. Rescaling of metal oxide nanocrystals for energy storage having high capacitance and energy density with robust cycle life. *Proc. Natl. Acad. Sci. USA* **112**, 7914–7919 (2015).
51. Jiang, W. et al. Ternary hybrids of amorphous nickel hydroxide-carbon nanotube-conducting polymer for supercapacitors with high energy density, excellent rate capability, and long cycle life. *Adv. Funct. Mater.* **25**, 1063–1073 (2015).
52. Ren, W., Zhang, H., Guan, C. & Cheng, C. Ultrathin MoS₂ nanosheets@metal organic framework-derived n-doped carbon nanowall arrays as sodium ion battery anode with superior cycling life and rate capability. *Adv. Funct. Mater.* **27**, 1702116 (2017).
53. Shan, T. T. et al. Combining nitrogen-doped graphene sheets and MoS₂: a unique film-foam-film structure for enhanced lithium storage. *Angew. Chem.* **55**, 12783–12788 (2016).
54. Mahmood, Q. et al. Transition from diffusion-controlled intercalation into extrinsically pseudocapacitive charge storage of MoS₂ by nanoscale heterostructuring. *Adv. Energy Mater.* **6**, 1501115 (2016).
55. Zhong, Y. et al. Transition metal carbides and nitrides in energy storage and conversion. *Adv. Sci.* **3**, 1500286 (2016).
56. Mai, L. Q. et al. Synergistic interaction between redox-active electrolyte and binder-free functionalized carbon for ultrahigh supercapacitor performance. *Nat. Commun.* **4**, 2923–2930 (2013).

Acknowledgements

This work was financially supported by National Natural Science Foundation (21273161), Natural Science Foundation of Shanghai (17ZR1447800), the Program for Professor of Special Appointment (Eastern Scholar) at Shanghai Institutions of Higher Learning, Hundred Youth Talent Plan of Tongji University, and the Fundamental Research Funds for the Central Universities.

Author contributions

N.F. and J.Y. conceived the ideas. R.M. investigated the polymers. N.F. and R.M. carried out intercalation experiments. N.F., R.M., L.Z., and Y.F. synthesized and characterized

the structure and composition of materials. N.F. and C.P. assembled the cells and conducted the measurements. N.F., R.M., L.Z., J.H., G.L., B.C., and J.Y. prepared the figures, analyzed the electrochemical data, and proposed the mechanism. N.F. and J.Y. co-wrote the manuscript. All the authors discussed the results and commented on the manuscript at all stages.

Additional information

Supplementary Information accompanies this paper at <https://doi.org/10.1038/s41467-019-09384-7>.

Competing interests: The authors declare no competing interests.

Reprints and permission information is available online at <http://npg.nature.com/reprintsandpermissions/>

Journal peer review information: *Nature Communications* thanks Jun Xu and the other anonymous reviewers for their contribution to the peer review of this work. Peer reviewer reports are available.

Publisher's note: Springer Nature remains neutral with regard to jurisdictional claims in published maps and institutional affiliations.



Open Access This article is licensed under a Creative Commons Attribution 4.0 International License, which permits use, sharing, adaptation, distribution and reproduction in any medium or format, as long as you give appropriate credit to the original author(s) and the source, provide a link to the Creative Commons license, and indicate if changes were made. The images or other third party material in this article are included in the article's Creative Commons license, unless indicated otherwise in a credit line to the material. If material is not included in the article's Creative Commons license and your intended use is not permitted by statutory regulation or exceeds the permitted use, you will need to obtain permission directly from the copyright holder. To view a copy of this license, visit <http://creativecommons.org/licenses/by/4.0/>.

© The Author(s) 2019